ARTICLE

# Revealing hidden features of a Japanese articulated iron lobster via non-destructive local element analysis and 3D imaging

Received 00th January 20xx,
Accepted 00th January 20xx

DOI: 10.1039/ D1JA00261A

László Szentmiklósi*[a], Zoltán Kis[a], Manako Tanaka[b], Boglárka Maróti[a], Masato Hoshino[c], Katalin Bajnok[a]

We present a workflow to non-destructively determine the elemental compositions of internal volumes of interest enclosed within complex-shaped objects, by combining 3D X-ray or neutron imaging, prompt-gamma activation analysis, and advanced Monte Carlo computer simulations. The correction of neutron- and gamma-attenuation effects during element analysis made it possible for the first time to obtain quantitative elemental compositions for such geometries. We applied the method successfully on an articulated iron lobster artifact from Edo period Japan. Using synchrotron X-ray and neutron imaging, we revealed that it has been constructed from numerous hammered plates. Rivets and two kinds of solder were identified based on the contrasts observed in the XCT images; these were selected for local composition analysis. It was found that one soldering material consisted of Cu63Zn37 brass, while the other was a eutectic tin and lead alloy Sn39Pb61. The Zn/Cu adhesive is widely used to bond small areas, whereas Sn/Pb adhesive is used for attaching larger surfaces.

## Introduction

During peaceful periods from the mid-Edo period (17$^{th}$ century) Japan, makers of samurai armor used their exceptional anatomic knowledge and metalwork skills to manufacture articulated animal sculptures called in Japanese *jizai okimono*. These are sophisticated standing ornaments of animals and mythological beasts made of iron, and with movable parts, limbs, joints, genuinely imitating the living creatures and served as gifts to their lords (*daimyo*) to evidence of the craftsmanship excellence of the master. In the late 19$^{th}$ century, bronze and silver articulated animal sculptures started to be made for export purposes. However, many details of the manufacturing process and the materials used in these elaborated metal objects are nowadays still unknown, as the knowledge was secretly passed on within the families from generation to generation.

Advanced composition and structure analysis techniques available at large-scale facilities, such as synchrotrons and neutron centres, are capable of characterizing such valuable artifacts non-destructively[1–4]. While optical photons and X-rays can penetrate a few (hundred) µm into metals[5], neutrons and gamma rays have an information depth up to a few mm-cm[6], so they offer either bulk representativity in case of homogeneous samples[7] or local concentrations relevant to an internal gauge volume for non-homogeneous objects[8], even if this volume element is inaccessible from outside [9,10,11,12].

A combination of synchrotron X-ray and neutron imaging as well as the prompt-gamma activation analysis[7], a neutron-based non-destructive element analysis technique, was selected to characterize this articulated iron lobster attributed to the famous master Myochin Munenaga (Fig. 1). The diameter of the artifact is 35 mm, while its total length is 230 mm. Like in an industrial reverse engineering exercise, we aimed at clarifying the fine details of the inner structure, visualize the structural connections, and analyze the material compositions of the object, to bridge the knowledge gap and provide evidence to re-establish these accurate metalwork techniques.

## Experimental

The lobster's structure was first studied using synchrotron X-ray microtomography at BL28B2 in SPring-8, Japan [13]. It was the first-ever attempt to investigate such articulated animal sculptures using X-ray CT. Here we took advantage of the high spatial resolution and the energetic X-rays offered by the synchrotron imaging. High-energy X-rays with the peak energy of around 200 keV were extracted from a white beam using heavy metal absorbers composed of tungsten with a thickness of 500 µm and lead with a thickness of 2 mm.


Fig. 1. The photo of the articulated iron lobster under study.

[a] Centre for Energy Research, 29-33 Konkoly-Thege Miklós street, Budapest, Hungary
[b] Showa Women's University, Department of History and Culture, 1-7-57 Taishido, Setagaya-ku, Tokyo 154-8533 Japan
[c] Japan Synchrotron Radiation Research Institute, 1-1-1 Kouto, Sayo-cho, Sayo-gun, Hyogo 679-5198 Japan

† Footnotes relating to the title and/or authors should appear here.
Electronic Supplementary Information (ESI) available: [details of any supplementary information available should be included here]. See DOI: 10.1039/x0xx00000x

The imaging setup was equipped with a conventional microtomographic stage and a visible-light conversion type X-ray imaging detector. It consisted of a Hamamatsu Photonics C11440-36U CMOS camera (native pixel size: 5.86µm×5.86µm, 1920(H)×1200(V) pixels), a lens system, and a 20µm thick Gadox ($Gd_2O_2S:Tb^+$) scintillator. The effective pixel size was 17.09µm×17.09µm, resulting in an effective field of view: 32.8 mm(H)×1.5 mm(V) at a sample-to-detector distance of 2.7 m when a magnification factor in the lens system was set to 0.33. The vertical field of view has been limited by the beam size, so 86 scans were merged to cover the whole object. During each of these CT scans, 1800 projections of 200 ms exposure times were taken over 180 degrees of rotation. The whole CT dataset was acquired for 41 500 s. The tomogram was obtained from these raw data with homemade software employing the conventional filtered back-projection method [14] and the parallel beam approximation.

It became clear that the articulated iron lobster has been constructed of numerous hammered plates and those were fixed with rivets and two kinds of soldering materials that produced different contrasts in the XCT images. Based on this knowledge, the local elemental compositions of the metal body and the solder materials were determined at the NIPS-NORMA facility[15] of the Budapest Neutron Centre (BNC) with position-sensitive, radiography-driven prompt-gamma activation analysis (PGAA). Being a bulk-analytical technique, even the regions of interest confined by the steel plates are amenable to composition measurement, unlike with the more common surface-probing analytical techniques, such as XRF, PIXE, LIBS, or LA-ICP-MS. Moreover, the object is covered with a brownish patina (*niiro*) that can bias the results of such analyses, while it does not influence significantly the PGAA data.

After mounting the object onto the computer-controlled xyzω sample stage, dynamic neutron radiography was used as real-time visual feedback for sample positioning [9]. Four positions were selected for compositional analysis based on the contrasts observed in the XCT: an area for Solder type 1, near the limbs of the lobster (Pos 1), an area where both Solder types are assumed to be present (Pos 2), an area representing the wall material only (Pos 3), and a spot around the eyes, representing Solder type 2 (Pos 4). These positions are depicted in Fig. 2. We took PGAA spectra for 10 000-13 000 s at Pos 1, Pos 3 and Pos 4, while an overnight measurement for 56000 s was completed at Pos 2. The obtained raw PGAA spectra are presented in Figure 3. They were processed with Hypermet-PC gamma spectroscopy program [16] and ProSpeRo [17] concentration calculation software.

The cross-section of the impinging neutron beam could be set with a computer-controlled neutron aperture to laterally confine the source of the analytical information.

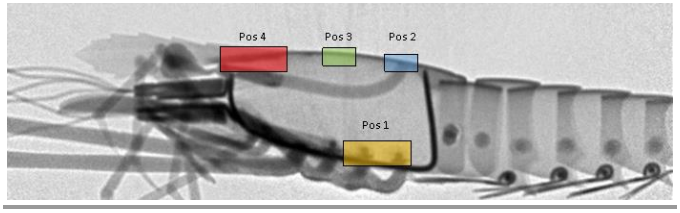


Fig. 2. Measurement positions for the position-sensitive PGAA experiment overlaid on the neutron radiogram.

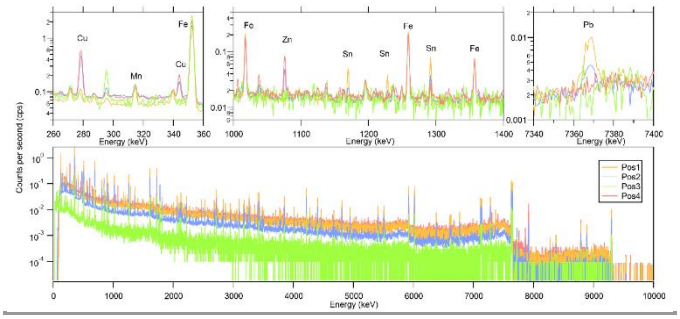


Fig. 3. The prompt-gamma spectra of the four measurement positions. Significant peaks of the elements are labeled in the insets.

As the analytical signal, i.e. the emission rate of the capture gamma-rays is proportional to the number of atoms of the element of interest present in the given infinitesimal volume and the local neutron flux.

In this chord geometry, the beam passes through the entire object towards the beam stop, and prompt-gamma photons are emitted along the beam path wherever material falls in the gauge volume. Our analytical goal is to decipher this integral information and determine the compositions of the individual materials using computer simulations and the geometry taken from the CT.

## Monte Carlo simulations

The most accurate way to follow the propagation of the neutrons and gamma-rays in a given experimental geometry is the use of Monte Carlo calculations. We used the MCNP 6.2 code [18] with the nuclear data library Lib80x [19] (based on ENDF/B-VIII.0). We implemented the detailed geometry of the Budapest Neutron Centre's NIPS-NORMA station in the MCNP simulation environment, including the sample chamber, the shielding, and the detector. The energy distribution of the neutron beam was taken from our earlier publication [20].

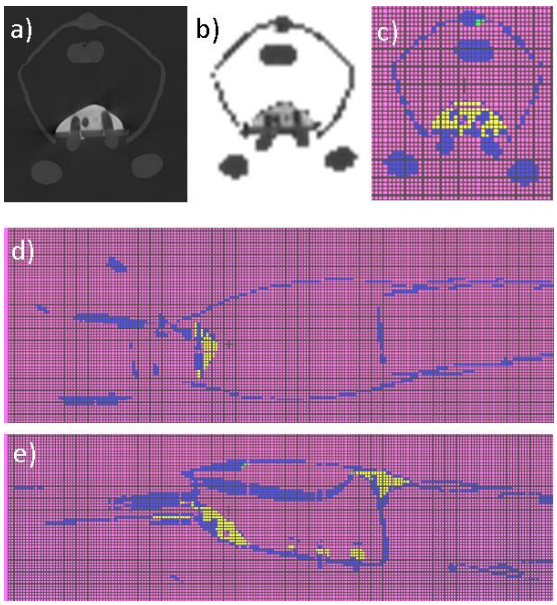


Fig. 4. The XCT slices (a) were segmented to discrete materials (b) and converted to the 3D MCNP simulation geometry, shown at cutting planes (c-e). Materials are color-coded: air (purple), metal body (blue), solder 1 (yellow) and solder 2 (green).

 

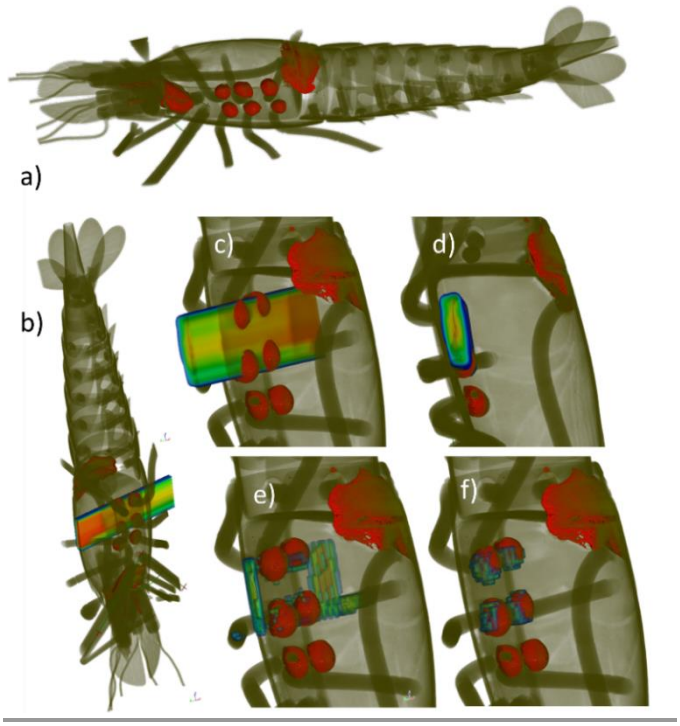


Fig. 5. The semi-transparent rendering of the lobster's structure, where the segmented soldering materials, identified by the XCT grayscale range, are shown in red (a). The Monte Carlo-calculated neutron beam intensity (b-d), as well as the emission maps of Fe (wall) (e) and Sn (solder) (f) for measurement position 1, are overlaid. Additional images are available in the Electronic Supplementary Information.

The MCNP calculation procedure has been recently validated for flat layered metal samples [21]. Here we further developed this approach to handle irregularly shaped and non-homogeneous objects via voxelization. The detailed geometry of the object was taken from segmented synchrotron CT data (Fig 4. a), where the distinct materials of the object were identified based on grayscale ranges (Fig 4. b). The material distribution was converted to a simulation geometry using a purpose-made utility [22]. The regular mesh of 66×102×278 voxels had unit voxel sizes of 0.5×0.5×0.5 $mm^3$ and was filled with four kinds of materials: air (purple), metal body (blue), solder 1 (yellow), and solder 2 (green), as illustrated in Fig. 4 c)-e). The material compositions were defined based on the raw PGAA concentration data.

The neutron intensity maps and the neutron capture rate maps for all relevant elements and all four measurement positions were simulated with a spatial resolution of 0.25 mm as a 3D superimposed mesh grid. The neutron capture rate map, normalized to the case of the undisturbed neutron beam, gave an integral quantity relevant to the neutron-related matrix-effect of the given element (self-shielding). In the second step of the simulation, these neutron capture rates of the elements were converted to emission maps of prompt-gamma rays, and the attenuation of the gamma-rays in the given measurement geometry towards the detector (self-absorption) was assessed [22]. The MCNP neutron simulations took 2 hours per irradiation position using 20 threads of an Intel i9-7940X 3.1 GHz workstation, while the corresponding gamma simulations lasted for 3 hours, for each relevant element in each of the four measurement positions.

## Results and Discussion

Based on the XCT data, the metal body and two kids of soldering materials could be visually differentiated. The full 3D rendering of the solder materials in red is shown in Figure 5. The voxelized results of the Monte Carlo simulations are presented here with intensity heat maps. Note that the neutron beam passes through the entire object, and more than one structural component may emit gamma rays from a single gauge volume. The emission maps of elements Fe (the main constituent of the metal body) and Sn (solder component) are plotted in Figures 5 e) and f), while further plots are available as Electronic Supplementary Information. Using these simulations, we achieved for the first time quantitative matrix-effect correction for such a non-homogeneous and complex-shaped object, which was a prerequisite to an unbiased local, but also in-depth element analysis by PGAA.

In PGAA spectra, most elements have several analytical lines at different energies, so there is an inherent way to verify the consistency of the calculations. In the ProSpeRo software [17], we obtain the masses of the elements based on the weighted averages of up to 25 analytical lines per element. The element-dependent correction factors for neutron self-shielding and gamma self-absorption obtained from the Monte Carlo calculations were introduced to replace the default correction method applicable only to homogeneous slab geometry. As a result of the improved corrections, self-consistent element masses could be derived from multiple analytical lines, even in such complex experimental geometry. This is evidenced by Fig. 6, where the masses of iron are plotted as a function of the gamma-energy of the analytical peaks.

Consistency was not only achieved within one PGAA spectrum (i.e. the mass of an element calculated from its low- and high-energy peaks agreed, see the blue data points in Fig. 6) but also between the several measurement positions (the compositions of the metal body and two kinds of solder materials obtained from different spectra also agreed, see Table 1). If we assume that two or three distinct materials are present in the gauge volume in different combinations, one can deduce the compositions of the body and the two solder types as listed in Table 1.

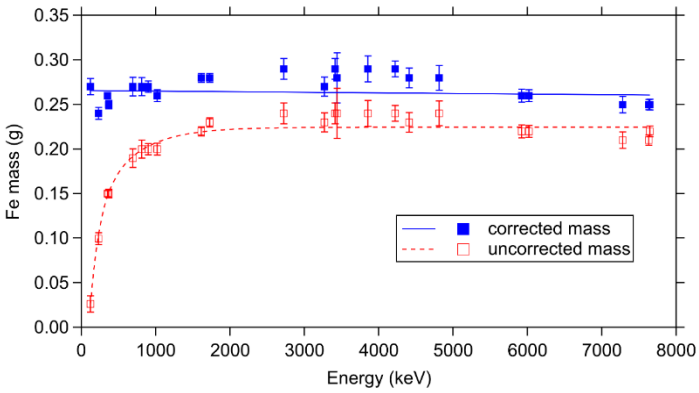


Fig. 6. The corrected and uncorrected masses of the element iron in Pos 4, as calculated from analytical lines at different prompt-gamma energies.

ARTICLE

| Element | Pos 1 | | Pos 2 | | Pos 3 | | Pos 4 | |
|---|---|---|---|---|---|---|---|---|
| | Lobster base metal + Solder 1 | | Lobster base metal + Solder 1 + Solder 2 | | Lobster base metal only | | Lobster base metal + Solder 2 | |
| | m/m% | rel. unc | m/m% | rel. unc | m/m% | rel. unc | m/m% | rel. unc |
| **Mn** | 0.37 | 3.0 | 0.45 | 2.9 | 0.42 | 3.0 | 0.47 | 6. |
| **Fe** | 99.63 | 0.03 | 99.55 | 0.03 | 99.58 | 0.03 | 99.53 | 0.03 |
| **Cu** | | | 61 | 1.3 | | | 63 | 1.2 |
| **Zn** | | | 39 | 2.0 | | | 37 | 2.1 |
| **Sn** | 27 | 4. | 27 | 6. | | | | |
| **Pb** | 73 | 1.6 | 73 | 2.1 | | | | |

Table 1. Element mass fractions and 1-sigma relative uncertainties of the metal body and the two soldering materials, as determined at the four measurement positions.

It was found that the lobster was made of 99.6% Fe with a 0.4% Mn impurity. Two soldering materials were identified: one is consisted of Cu63Zn37 brass, while the other is eutectic tin and lead alloy Sn39Pb61. Zn/Cu adhesive is widely used to bond small areas, whereas Sn/Pb adhesive is used for attaching larger surfaces.

## Conclusions

We successfully characterized for the first time the internal structure and the material composition of a Japanese articulated metal lobster. This was made possible by using synchrotron X-ray tomography, neutron radiography experiments for geometry characterization, and position-sensitive prompt-gamma activation analysis, supported by advanced Monte Carlo calculations, for elemental composition measurements.

The joint consideration of position-sensitive PGAA element analysis and imaging data allows a more reliable explanation of the so far independently treated results. Moreover, the quantitative matrix-effect correction we developed in the course of this work made it possible to obtain consistent elemental concentrations within each spectrum, and also over the several measurement spots, even if the regions of interest are not accessible from outside, i.e. not amenable to the more conventional surface-confined analytical techniques.

Using these data, we concluded that the body of the lobster is pure iron with 0.4% Mn impurity, whereas two soldering materials, Cu63Zn37 brass, and eutectic Sn39Pb61 alloy were identified. The outcome of this reverse engineering study paves the way to re-establish the lost skills of the late Japanese masters, while, on the other hand, the developed analytical methodology will be applicable well beyond the scope of the current study.

## Author Contributions

László Szentmiklósi – Conceptualization, Investigation, Methodology, Supervision, Funding acquisition, Visualization, Writing – original draft

Zoltán Kis – Investigation, Methodology, Software, Data curation, Writing – review & editing

Manako Tanaka – Conceptualization, Investigation, Supervision, Funding acquisition, Writing – review & editing

Boglárka Maróti – Investigation, Formal Analysis, Validation, Writing – review & editing

Masato Hoshino – Investigation, Methodology, Data curation, Formal analysis, Writing – review & editing

Katalin Bajnok – Project administration, Writing – review & editing

## Conflicts of interest

There are no conflicts to declare.

## Acknowledgments

The experiment performed at the Budapest Neutron Centre was a part of project No. 124068 that has been implemented with financial support from the National Research, Development and Innovation Fund of Hungary, financed under the K_17 funding scheme. L. Sz. acknowledges the financial support of the János Bolyai Research Fellowship of the Hungarian Academy of Sciences.

The X-ray microtomography experiments were performed at the BL28 of SPring-8 with the approval of the Japan Synchrotron Radiation Research Institute (JASRI) (Proposal No. 2016B1799、2016B1798、2017A1718、2017B1867). M.T acknowledges the financial supports from JSPS KAKENHI Grant Number 26702004, JST COI Grant Number JPMJCE1308, and Showa Women's University Grant-in-Aid for Research Projects. The authors are grateful to K. Harada, the owner of the articulated iron lobster, N. Yagi and K. Uesugi for technical assistance with the X-ray microtomography experiments.

## Notes and references

1 S. Sanchez, P. E. Ahlberg, K. M. Trinajstic, A. Mirone and P. Tafforeau, Three-Dimensional Synchrotron Virtual Paleohistology: A New Insight into the World of Fossil Bone Microstructures, *Microsc. Microanal.*, 2012, **18**, 1095–1105.

2 A. Pradel, M. Langer, J. G. Maisey, D. Geffard-Kuriyama, P. Cloetens, P. Janvier and P. Tafforeau, Skull and brain of a 300-million-year-old chimaeroid fish revealed by synchrotron holotomography, *Proc. Natl. Acad. Sci.*, 2009, **106**, 5224–5228.

3 M. D. de Jonge, C. Holzner, S. B. Baines, B. S. Twining, K. Ignatyev, J. Diaz, D. L. Howard, D. Legnini, A. Miceli, I. McNulty, C. J. Jacobsen and S. Vogt, Quantitative 3D elemental microtomography of Cyclotella meneghiniana at 400-nm resolution, *Proc. Natl. Acad. Sci.*, 2010, **107**, 15676–15680.

4 T. Swanston, T. L. Varney, M. Kozachuk, S. Choudhury, B. Bewer, I. Coulthard, A. Keenleyside, A. Nelson, R. R. Martin, D. R. Stenton and D. M. L. Cooper, Franklin expedition lead exposure: New insights from high resolution confocal x-ray fluorescence imaging of skeletal microstructure, *PLoS One*, 2018, **13**, e0202983.

5 S. Choudhury, D. N. Agyeman-Budu, A. R. Woll, T. Swanston, T. L. Varney, D. M. L. Cooper, E. Hallin, G. N. George, I. J. Pickering and I. Coulthard, Superior spatial resolution in confocal X-ray techniques using collimating channel array optics: elemental mapping and speciation in archaeological human bone, *J. Anal. At. Spectrom.*, 2017, **32**, 527–537.

6 T. Belgya, Z. Kis, L. Szentmiklósi, Z. Kasztovszky, P. Kudejova, R. Schulze, T. Materna, G. Festa and P. A. Caroppi, First elemental imaging experiments on a combined PGAI and NT setup at the Budapest Research Reactor, *J. Radioanal. Nucl. Chem.*, 2008, **278**, 751–754.

7 G. L. Molnár, *Handbook of Prompt Gamma Activation Analysis : with Neutron Beams*, Springer US, 2004.

8 R. Schulze, L. Szentmiklósi, P. Kudejova, L. Canella, Z. Kis, T. Belgya, J. Jolie, M. Ebert, T. Materna, K. T. Biró and Z. Hajnal, The ANCIENT CHARM project at FRM II: Three-dimensional elemental mapping by prompt gamma activation imaging and neutron tomography, *J. Anal. At. Spectrom.*, 2013, **28**, 1508–1512.

9 L. Szentmiklósi and Z. Kis, Characterizing nuclear materials hidden in lead containers by neutron-tomography-driven prompt gamma activation imaging (PGAI-NT), *Anal. Methods*, 2015, **7**, 3157–3163.

10 L. Szentmiklósi, B. Maróti, Z. Kis and Z. Kasztovszky, Integration of neutron-based elemental analysis and imaging methods and applications to cultural heritage research, *J. Archaeol. Sci. Reports*, 2018, **20**, 476–482.

11 E. Abraham, M. Bessou, A. Ziéglé, M.-C. Hervé, L. Szentmiklósi, Z. Kasztovszky, Z. Kis and M. Menu, Terahertz, X-ray and neutron computed tomography of an Eighteenth Dynasty Egyptian sealed pottery, *Appl. Phys. A*, 2014, **117**, 963–972.

12 E. Mauerhofer and A. Havenith, The MEDINA facility for the assay of the chemotoxic inventory of radioactive waste packages, *J. Radioanal. Nucl. Chem.*, 2014, **302**, 483–488.

13 M. Hoshino, K. Uesugi, R. Shikaku and N. Yagi, High-energy, high-resolution x-ray imaging for metallic cultural heritages, *AIP Adv.*, 2017, **7**, 105122.

14 A. C. Kak and M. Slaney, *Principles of Computerized Tomographic Imaging*, Society for Industrial and Applied Mathematics, 2001.

15 Z. Kis, L. Szentmiklósi and T. Belgya, NIPS–NORMA station—A combined facility for neutron-based nondestructive element analysis and imaging at the Budapest Neutron Centre, *Nucl. Instruments Methods Phys. Res. Sect. A Accel. Spectrometers, Detect. Assoc. Equip.*, 2015, **779**, 116–123.

16 B. Fazekas, T. Belgya, L. Dabolczi, G. Molnár and A. Simonits, HYPERMET-PC: Program for automatic analysis of complex gamma- ray spectra, *J. Trace Microprobe Tech.*, 1996, **14**, 167–172.

17 Z. Révay, Determining Elemental Composition Using Prompt γ Activation Analysis, *Anal. Chem.*, 2009, **81**, 6851–6859.

18 R. F. Fleming, Neutron self-shielding factors for simple geometrics, *Int. J. Appl. Radiat. Isot.*, 1982, **33**, 1263–1268.

19 J. Lloyd Conlin, W. Haeck, D. Neudecker, D. Kent Parsons and M. C. White, *LA-UR-18-24034: Release of ENDF/B-VIII.0-Based ACE Data Files*, Los Alamos, 2018.

20 T. Belgya, Z. Kis and L. Szentmiklósi, Neutron Flux Characterization of the Cold Beam PGAA-NIPS Facility at the Budapest Research Reactor, *Nucl. Data Sheets*, 2014, **119**, 419–421.

21 L. Szentmiklósi, B. Maróti and Z. Kis, Prompt-gamma activation analysis and neutron imaging of layered metal

structures, *Nucl. Instruments Methods Phys. Res. Sect. A Accel. Spectrometers, Detect. Assoc. Equip.*, 2021, **1011**, 165589.

22 L. Szentmiklósi, Z. Kis, B. Maróti and L. Z. Horváth, Correction for neutron self-shielding and gamma-ray self-absorption in prompt-gamma activation analysis for large and irregularly shaped samples, *J. Anal. At. Spectrom.*, 2021, **36**, 103–110.

 